



Article

Particle Size Distribution Slope Changes along the Yellow River Delta Observed from Sentinel 3A/B OLCI Images

Song Jin ¹, Tao Zou ¹, Qianguo Xing ^{1,*} , Xiangyang Zheng ¹ and Sergio Fagherazzi ²

¹ CAS Key Laboratory of Coastal Environmental Processes and Ecological Remediation, Yantai Institute of Coastal Zone Research, Chinese Academy of Sciences, Yantai 264003, China; songjin@yic.ac.cn (S.J.)

² Department of Earth and Environment, Boston University, Boston, MA 02215, USA

* Correspondence: qgxing@yic.ac.cn

Abstract: Quantitative estimates of particle size in estuaries and shelf areas are important to understand ocean ecology and biogeochemistry. Particle size can be characterized qualitatively from satellite observations of ocean color. As a typical marginal sea, the Yellow River Delta (YRD) with the Bohai Sea experiences a complex hydrodynamic environment. Here, we attempt to quantify the particle size distribution (PSD) slope (ζ) based on its relationship with the particle backscattering exponent from Sentinel-3A/B OLCI. The PSD slope, ζ displays temporal and spatial variability in the YRD with the Bohai Sea. Its value varies between 3 and 4, and typically exceeds 5 in offshore areas. The lowest value of ζ occurs in the winter, indicating the presence of fine inorganic particles in the water, while high values are attained in the spring, when phytoplankton blooms increase the particle size. ζ decreases near the river mouth because of the large sediment-laden discharge debouching into the sea. We detected a slight increase in ζ when turbid waters were present in the period 2016–2022. Environmental factors, such as sea surface temperature, sea surface wave height, and wind, may control particle size and ζ in the long term. Inorganic suspended particle matter is derived along the YRD using the magnitude of ζ . The mean inorganic suspended particle matter area in winter approaches 23,900 km² when $\zeta < 4.6$. This study thoroughly characterizes variations in ζ in the YRD with the Bohai Sea and clarifies the contributions of driving factors from human activities and climate change.



Citation: Jin, S.; Zou, T.; Xing, Q.; Zheng, X.; Fagherazzi, S. Particle Size Distribution Slope Changes along the Yellow River Delta Observed from Sentinel 3A/B OLCI Images. *Remote Sens.* **2024**, *16*, 938. <https://doi.org/10.3390/rs16060938>

Academic Editor: SeungHyun Son

Received: 7 January 2024

Revised: 25 February 2024

Accepted: 5 March 2024

Published: 7 March 2024



Copyright: © 2024 by the authors. Licensee MDPI, Basel, Switzerland. This article is an open access article distributed under the terms and conditions of the Creative Commons Attribution (CC BY) license (<https://creativecommons.org/licenses/by/4.0/>).

Keywords: remote sensing; particle size distribution slope; Yellow River Delta; Sentinel-3A/B OLCI; environmental factor

1. Introduction

Suspended particulates, such as phytoplankton, heterotrophic organisms, or detrital sediment, play an important role in biogeochemical cycling in marine environments [1–3]. Particle size is one of the fundamental particle parameters to describe the behavior of particle physical conditions. On the one hand, particle size may alter trophic relations within planktonic algae community diversity [4]. Moreover, horizontal and vertical fluxes of elements in the water column also depend on particle size, as this parameter controls settling velocities [5,6]. The size distribution of organic-dominated and inorganic-dominated particles has significant characteristic differences owing to particle composition, internal structure, and shape [7,8]. Inorganic-dominated particles, especially mineral sediment, prevail on the shelf while algae cells and other biological detritus are mainly present in the pelagic area [9,10]. Therefore, exploring particle size distribution is of significance to assess coastal and inland water quality.

Because measuring individual particle size remains challenging, the particle size distribution function (PSD) can be used to count particle size frequency in given size classes [11]. The PSD can affect the scattering properties of polydispersion in seawater once a specific size range (lower and upper size) is chosen [12,13]. Single-term forms,

including power-law function, Gaussian and Gamma functions, or multiple-term forms such as multisegmented hyperbolic distribution are common PSD distributions [14]. The power-law model is one of the most popular methods in characterizing particle size in marine systems. This model provides a good fit with a hyperbolic curve and the PSD slope (ζ) varies between 2.5 and 5 [15]. Low values of ζ and high particle concentrations are dominant in estuarine waters and high values of ζ that represent low particle concentrations are characteristic of the open sea [16]. Therefore, a simple approximation of ζ can be successfully used to characterize particle distribution in estuarine water.

Directly measuring PSD using the available instruments presents limitations in specific ranges of particle size, so a straightforward and quantitative description of particle size distribution is difficult [10]. The PSD in marine environments is related to inherent optical proxies, and the latter are relatively simple to measure over large scales with remote sensing [17,18]. It is of interest to quantitatively link optical proxies and the PSD parameters. The size and shape of attenuation spectra ($c_p(\lambda)$) is directly linked to the shape of the PSD for polydispersion using Mie scattering theory [19]. Spectral backscattering can provide particle size properties from in situ measurements [20]. Optical proxies enable the development of bio-optical algorithms, and appropriate optical proxies can describe the spatial and temporal variability of the PSD [12,21]. $c_p(\lambda)$ is governed by forward scattering and cannot be easily calculated from satellite measurements [5,22]. However, the spectral slope of particle backscattering (η) shows a high correlation with ζ [5]. For instance, for weak absorbing mineral particles, η increases from 0.09 to 1.62 while ζ varies from -3.2 to -4.8 . And η is sensitive to particles with diameter less than $10\ \mu\text{m}$ [23]. Considering that the particle backscattering coefficients ($b_{bp}(\lambda)$) can be estimated using a Quasi-Analytical Algorithm (QAA), it is natural to qualify and quantify the marine PSD using the parameter η . In this way satellite images, such as MODIS, VRIIS and Sentinel 3A/B OLCI, can be used to characterize the PSD [4,24,25]. These images are informative in terms of estimating the time series of the temporal and spatial patterns of the PSD slope, ζ , in the nearshore area.

As a classical research area, here we selected the Yellow River Delta (YRD) to characterize the PSD because it is an ecologically fragile region of the nearby shelf. The Yellow River is the second largest river in China, with a huge amount of terrigenous sediment input annually. The material suspended in the water column is significantly influenced by human activity and weather conditions. Seasonal changes, terrigenous discharge inputs, wind-induced waves and currents can directly influence the PSD in coastal and estuarine waters [26]. For example, sediment fining occurs when riverine floods bring large loads into the sea. The PSD coarsens during the passing of a typhoon because of energetic waves, and suspended sediments become finer when winds decrease [24]. The Sustainable Development Goals (SDG) are the blueprint for achieving a better and more sustainable future for all. As the focus of SDG 14 is marine sustainable development, clarifying the drivers of particle size variations has become the prerequisite for understanding marine changes [27]. This study aims to quantify the PSD variation in the YRD with the Bohai Sea through remote sensing techniques, and then explore the potential drivers that control PSD in coastal waters. Ultimately, we attempt to roughly distinguish the particles' type with the help of PSD based on our remote sensing results [28]. The findings of this study can improve our understanding of the characteristics of particle size in optically complex water types.

2. Materials and Methods

2.1. Study Area

The Yellow River delta (YRD) with the Bohai Sea is located in the western part of the Bohai Sea and encompasses parts of Bohai Bay, Yellow River estuary (YRE), and the Laizhou Bay (Figure 1). The study area is characterized by four distinct seasons influenced by the East Asia Monsoon. Moderate southerly winds ($3\text{--}6\ \text{m/s}$) prevail during summer months, while strong northerly winds ($>10\ \text{m/s}$) blow in winter triggering waves with a 1.25 average height [29]. An irregular semi-diurnal tide with a range of $0.6\text{--}0.8\ \text{m}$ is present in the river

estuary [30]. Moreover, there is a tidal residual circulation along the west coast of the Bohai Sea, exhibiting opposite directions in winter and summer times [31]. Although the Yellow River has the second largest sediment load in the world, its discharge and sediment load have already decreased by more than 80% over the last 60 years [32]. Peak discharges are concentrated in the summer, due to an artificial water and sediment regulation scheme (WSRS) [33]. Most of the YRD with the Bohai Sea is covered by fine sediments, including soft clay, silt mud, and coarse silt with a grain size of less than 100 nm [34]. Silt fractions account for approximately 45.22% of the surface sediment, and the average content of sand and clay is 36.19% and 18.33%, respectively [35].

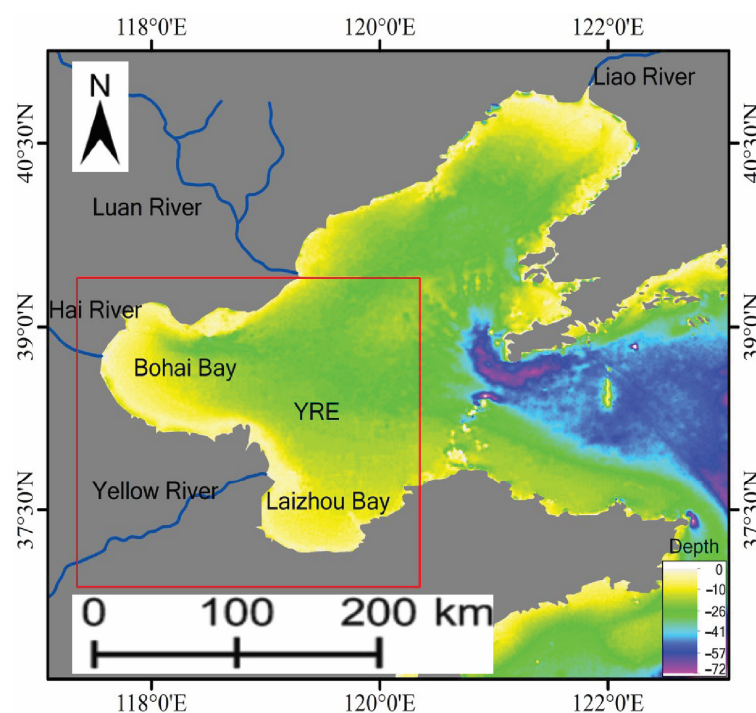


Figure 1. Study area. The red rectangle includes the Bohai Bay, Yellow River estuary (YRE) and Laizhou Bay.

2.2. Data Sources

Sentinel-3A/B OLCI images have been widely used to monitor water quality and harmful algae blooms in coastal areas and inland waters for its abundant bands, high revisit time and broad scanning swath. This sensor provides 21 bands with 300 m spatial resolution and 1270 km sweep swath with a 1–2 day revisit time [36]. The first ten bands have visible wavelengths (400–681.25 nm), and the latter eleven bands are NIR wavelengths (708.75–1020 nm). The Sentinel-3A/B L1 products can be downloaded from the Copernicus Open Access Hub (<https://dataspace.copernicus.eu>, accessed on 1 June 2023). The Management Unit of the North Sea Mathematical Models (MUMM) is implemented to remove atmospheric effects [37]. It is embedded in the SeaWiFS Data Analysis System (SeaDAS 8.2.0) software (<https://seadas.gsfc.nasa.gov/>, accessed on 1 June 2023). Briefly, the l2gen processor is used to generate Level-2 mapped rasters of all visible bands Rrs from the Level-1 top-of-atmosphere calibrated radiances through the standard multiple scattering and iterative near infrared (NIR) model [38]. A total of 522 Sentinel-3A/B images from 2016 to 2022 were used to extract the PSD slope. This MUMM performs very well in turbid coastal waters [39]. The clouds and sea ice are removed using the empirical method presented in [40].

To investigate factors influencing particle size, we analyzed the Yellow River runoff and sediment load at the Lijin hydrological station. The data are obtained from the Yellow River Conservancy Commission of the Ministry of Water Resources (<http://www.yrcc.gov.cn/>, accessed on 1 July 2023). In addition, monthly wind speed, sea surface temperature

(SST) and sea surface height (SSH) are directly collected from the fifth-generation Global Climate and Atmospheric Reanalysis Tool (<https://cds.climate.copernicus.eu/>, accessed on 1 July 2023).

2.3. Estimation of PSD Slope, ξ

Seawater backscattering, $b_b(\lambda)$ is the sum of backscattering of water molecules ($b_{bw}(\lambda)$) and particles ($b_{bp}(\lambda)$) (Equation (1)). $b_{bp}(\lambda)$ consists of planktonic components and suspended sediments. $b_w(\lambda)$ includes contributions from the forward and backward direction of seawater molecules relative to the incident light direction [41]. Therefore $b_{bw}(\lambda)$ is half of total $b_w(\lambda)$.

$$b_b(\lambda) = b_{bw}(\lambda) + b_{bp}(\lambda) \quad (1)$$

$b_{bp}(\lambda)$ can be computed with the Mie theory, which has already been adopted in ocean optics in the last few decades [42,43]. Individual particles are assumed as non-interacting homogeneous spheres and the Mie theory provides an estimate of the inherent particle optical properties [44,45]. $b_{bp}(\lambda)$ significantly depends on size parameters such as diameter, shape, volume and its complex refractive index with respect to the surrounding medium [12,46]. The corresponding coefficient in the selected wavelength is estimated by integration over all particle diameters (Equation (2)).

$$b_{bp}(\lambda) = \int_{D_{\min}}^{D_{\max}} \frac{\pi}{4} D^2 Q_{bb}(D, \lambda, m) N(D) dD \quad (2)$$

$Q_{bb}(D, \lambda, m)$ is the backscattering efficiency factor of a single particle with diameter D and refractive index (m) in relation to seawater. This parameter can be directly obtained using the Mie theory [42]. The power-law expression of the PSD is the following (Equation (3)).

$$N(D) = N_0 \left(\frac{D}{D_0} \right)^{-\xi} \quad (3)$$

where $N(D)$ represents the number of particles per volume normalized by the size bin width at a certain particle size D , N_0 denotes the particle differential number concentration at D_0 , and ξ is the power-law slope. The exponent of ξ is an ideal indicator to characterize particle sizes in highly turbid waters [47]. Values of ξ greatly depends on regional particle spatial and temporal variability and the smallest ξ is appointed as 2.7 [16].

$b_{bp}(\lambda)$ is a spectrally correlated parameter, so it fits the power law equation with the spectral slope η [48].

$$b_{bp}(\lambda) = b_{bp}(\lambda_0) \left(\frac{\lambda}{\lambda_0} \right)^{-\eta} \quad (4)$$

Considering the wavelengths of 754 and 865 nm are quite significant and valid in moderately turbid waters, the near-infrared bands of 754 and 865 nm are used in the calculation of the slope η [49,50]. η can be consequently calculated using the computed $b_{bp}(754)$ and $b_{bp}(865)$ (Equation (4)).

The absorption coefficient $a(\lambda)$ includes the absorption parameter for pure seawater ($a_w(\lambda)$), phytoplankton ($a_{ph}(\lambda)$), dissolved matter ($a_g(\lambda)$), and nonalgal particles $a_d(\lambda)$ [43]. The sum of $a_{ph}(\lambda)$, $a_g(\lambda)$ and $a_d(\lambda)$ is the non-water absorption coefficient in Equation (5). Water absorption $a_w(\lambda)$ dominates total absorption coefficient for longer wavelengths ($a_w(\lambda) \approx a(\lambda)$). For example, $a(754)$, $a(865)$ are 2.9 m^{-1} and 4.6 m^{-1} while $a_{ph}(\lambda)$, $a_g(\lambda)$ and $a_d(\lambda)$ at 754, 865 nm are normally negligible.

$$a(\lambda) = a_w(\lambda) + a_{ph}(\lambda) + a_g(\lambda) + a_d(\lambda) \quad (5)$$

In situ measurements of $R_{rs}(\lambda)$ can be used to express the subsurface remote sensing reflectance ($r_{rs}(\lambda)$) based on the air-water transmittance [51]:

$$r_{rs}(\lambda) = \frac{R_{rs}(\lambda)}{0.52 + 1.7R_{rs}(\lambda)} \quad (6)$$

$r_{rs}(\lambda)$ is analytically related to the ratio of total backscattering to the sum of total backscattering and total absorption. Using the constant model parameters $g_1(0.0949)$ and $g_2(0.0794)$ [45], the relationship can be represented as follows:

$$r_{rs}(\lambda) = g_1 \left(\frac{b_b(\lambda)}{a(\lambda) + b_b(\lambda)} \right) + g_2 \left(\frac{b_b(\lambda)}{a(\lambda) + b_b(\lambda)} \right)^2 \quad (7)$$

The slope of particle backscattering, η , is simply associated with the PSD slope ζ , and it is nearly equal to $\eta + 3$ [15]. Moreover, the relationship between η and ζ can also be mathematically represented as a third-degree polynomial fit for a wide range of η and ζ with high level of accuracy. The 490, 510 and 555 nm wavelengths are generated from a lookup table (LUT) using the Mie scattering model [17]. This function can be used in turbid inland and coastal waters [21].

$$\zeta = -0.00191\eta^3 + 0.127\eta^2 + 0.482\eta + 3.52 \quad (8)$$

Here, we first use two wavelengths of $R_{rs}(754)$, $R_{rs}(865)$ from the Sentinel 3A/B to compute $r_{rs}(754)$, $r_{rs}(865)$ based on Equation (6). Then, $b_b(754)$, $b_b(865)$ can be calculated when g_1 , g_2 , $a(754)$ and $a(865)$ are appointed using Equation (7). And η can be known since combining Equations (1) and (4). Finally, we can obtain ζ from Equation (8) through remote sensing technique. This algorithm has been successfully applied to several global classic coastal waters, such as Subei Shoal, Hangzhou Bay, Meghna River and Atchafalaya River [17,21]. Moreover, organic and fine inorganic suspended sediments can be distinguished by means of a given ζ . The threshold of ζ is determined by multiple manually trial from ζ mapping.

2.4. Particle Backscattering Ratio Using the Mie Scattering

The backscattering ratio $\tilde{b}_{bp}(\lambda)$ is calculated as follows:

$$\tilde{b}_{bp}(\lambda) = \frac{b_{bp}(\lambda)}{b_p(\lambda)} \quad (9)$$

The b_p is similar to b_{bp} in Equation (2), but scattering efficiency factors $Q_b(D, \lambda, m)$ participate in the calculation of b_p . The efficiency factor $Q_{bb}(D, \lambda, m)$ and $Q_b(D, \lambda, m)$ from the Mie theory are calculated with following refractive index of particle (m):

$$m = n - in' \quad (10)$$

where n is the real part of refractive index and n' is imaginary part of refractive index. The bulk refractive index n ranges from 1.02 to 1.2 at increments of 0.2 and n' is held constant at 0.005 when establishing the relationship between backscattering ratio and the exponent of power law of PSD using Equation (2). Then, we are able to compare the relationship between $\tilde{b}_{bp}(\lambda)$ and ζ with the changing n .

2.5. Time Series Analysis of the PSD Slope, ζ

In order to analyze changes in ζ , we introduce a method that decomposes remotely sensed ζ time series into trend, seasonal and residual components [52]. The seasonal-trend decomposition uses LOESS (STL), a robust method for time-series decomposition in

environmental analysis. The seasonal component represents a gradient change in particle size on a yearly time scale, which might include abrupt variations.

This signal can be used to study the effect of climate change, land use, and land management. The seasonal component is a regular and periodic variation in ζ at the annual scale. The residual component is the stochastic and irregular change in ζ induced by atmospheric conditions and extreme events (e.g., human activity, storms or flood events). The STL is simply the addition of the three components, so that:

$$T(t) = T_t(t) + T_s(t) + T_n(t) \quad (11)$$

$T_t(t)$, $T_s(t)$ and $T_n(t)$ are the trend, seasonal and residual components of ζ in time. The mean of ζ in the whole YRE is utilized in the trend analysis.

Meanwhile, a low-pass filter is performed on ζ and its related forcing parameters to explain potential environmental factors to particle size. It lets the low frequency components of signal to pass through and restrict high frequency, which make use of the desired measured (ζ , SSH, SST or wind speed) by removing signal noise [53].

3. Results

3.1. Daily Values of the PSD Slope, ζ

We selected four days to display ζ in different water and sediment conditions (Figure 2). The magnitude of ζ increases with offshore distance from the YRD, and the most significant gradient was present on 12 March and 21 May 2019 (Figure 2b). Turbid seawaters possess a lower ζ with respect to clear water. ζ is lower than 4 in the offshore area of the delta while it exceeds 5 in the eastern part of Bohai Sea. Two peaks of ζ occur in the frequency histogram, the left peak is located at 4 and a second peak is at 5.5 on those two days (Figure 2c). ζ is uniform on 9 September when the plankton biomass affects ζ in the whole sea (Figure 2b). On that day, the value of ζ is the highest (between 5.0 and 5.5). A high turbidity region parallel to the shoreline is present on 12 December (blue belt in Figure 2a,b). ζ in wintertime is a little lower than on the other three days (Figure 2c). The histogram morphology of ζ changes quickly in the spring and tends to stabilize in autumn. Generally, ζ varies both in space and magnitude along with in particles distribution.

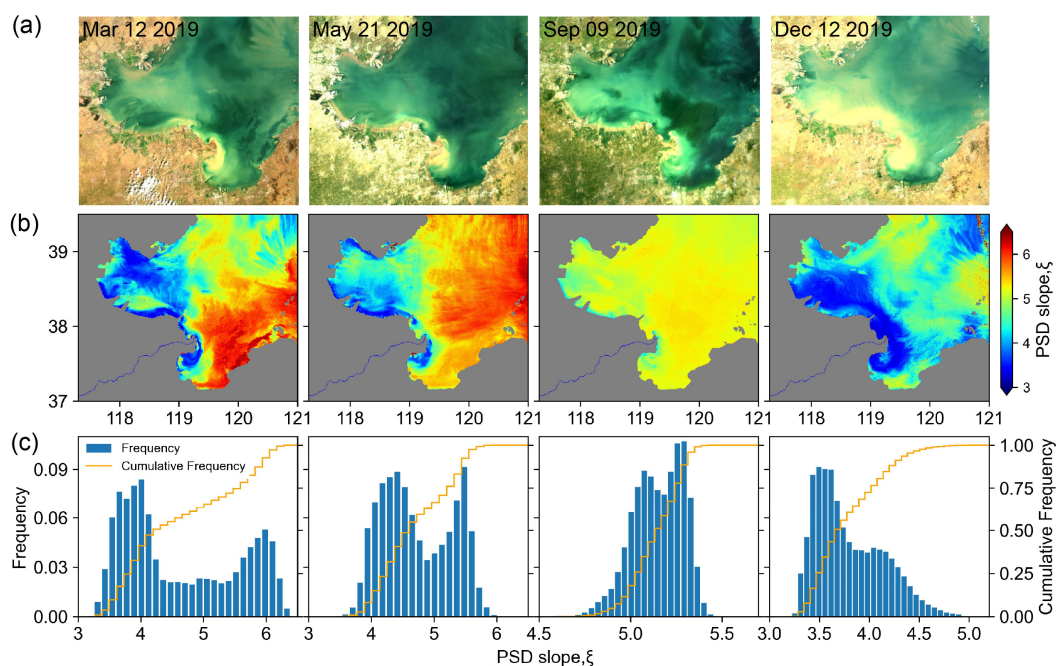


Figure 2. Daily PSD slope, ζ in the Yellow River Delta. (a) RGB images on 12 March, 21 May, 9 September and 12 December 2019. (b) Daily PSD slope, ζ . (c) Histogram of PSD slope, ζ in each day.

3.2. Interannual and Monthly Changes of the PSD Slope, ζ

The spatial distribution of the annual mean ζ presents variations in the last 7 years (Figure 3). The low value of ζ along the Bohai Bay coast also spills into Laizhou Bay. The ζ values along the coast are restricted to within 4 to 4.5, while they exceed 5 away from the turbid zone. It can be inferred that inorganic suspended solids (clay, silt) are predominant in coastal waters, due to resuspension of bottom sediments. The behavior of ζ shows similar patterns with sea depth considering the small value of ζ was the most consistent with the dispersion of shallow waters (Figure 1). The ζ in the Yellow River Estuary is persistently below 4 because of the fresh water injected into the Bohai Sea. A low ζ region was present in Bohai Bay in 2017, and the ζ was overall low in this year. The ζ changes little during 2018–2021, while a pronounced ζ band in the mid-south Bohai Sea was present in 2022. Influenced by Yellow River sediment input, a rotating water mass developed in Laizhou Bay with ζ values close to 4. In addition, the gradient of ζ within the Bohai also seems to have increased a little in the last three years.

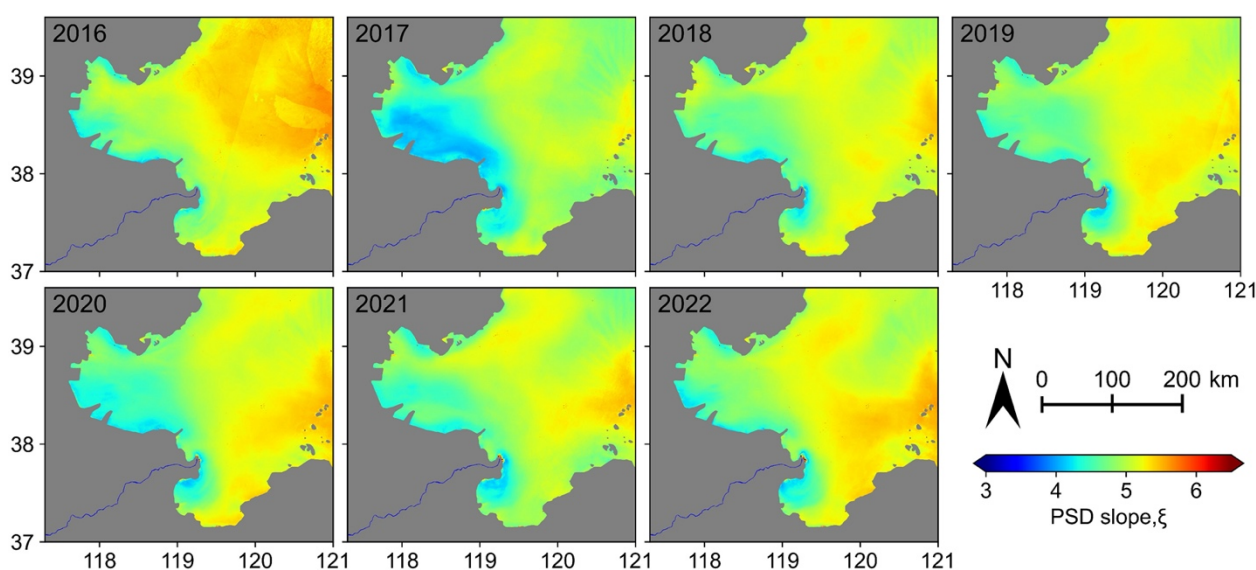


Figure 3. Annual PSD slope, ζ mapping during 2016–2022. Note that Sentinel 3A OLCI images are available since August 2016, ζ in this year is higher than in other years.

To analyze ζ variations, we calculated the monthly and annual values in three different regions: Bohai Bay, the YRE and Laizhou Bay. Considering ζ is usually greater than 2.7, we will directly note outliers when $\zeta < 2.65$ [16]. ζ in the Bohai Bay is low, with a median value of 4.5 (Figure 4a). The highest values occur in May and June. ζ in the estuary displays little change in this period, but there are many outliers in 2019–2021. The lowest value of ζ (2.02) was reached on 2 January 2021. ζ values in LaiZhou Bay display the highest variation in contrast to the Bohai Bay and YRE, but its median value is similar to the YRE (Figure 4c). Outlier values were mostly present in the YRE and LaiZhou Bay in 2019 and 2020. Moreover, the ζ in LaiZhou Bay presents many outliers because the ζ is not distributed homogeneously. For instance, the lowest ζ in Laizhou Bay is 2.633 on 4 June 2020 and 3.48 on 9 June 2016, while most values exceed 4.5 with the highest value of 7.33. As a result, PSD outliers are present in the warm season. In the cold season, ζ ranges from 3.6 to 5.0. A monthly ANOVA analysis was performed among the three regions (Figure 5). Significant differences in the monthly ζ derived from the ANOVA analysis are presented in the YRE and Bohai Bay, and Bohai Bay and LaiZhou Bay (p -value < 0.0001). There is no obvious differences between the YRE and LaiZhou Bay (Figure 5).

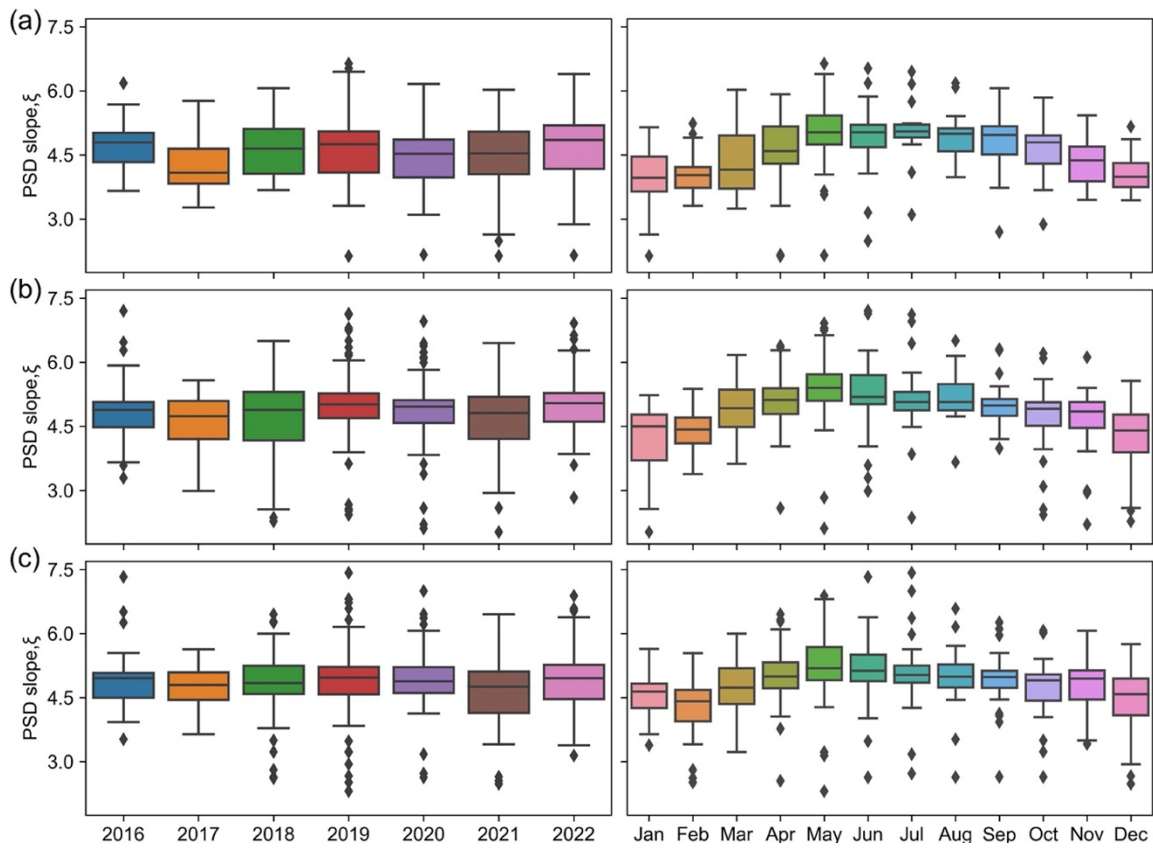


Figure 4. Annual and monthly variations in ζ at the front of the YRD. (a) Annual and monthly differences in ζ in Bohai Bay. (b) Annual and monthly differences in ζ in the YRE. (c) Annual and monthly differences in ζ in the Laizhou Bay.

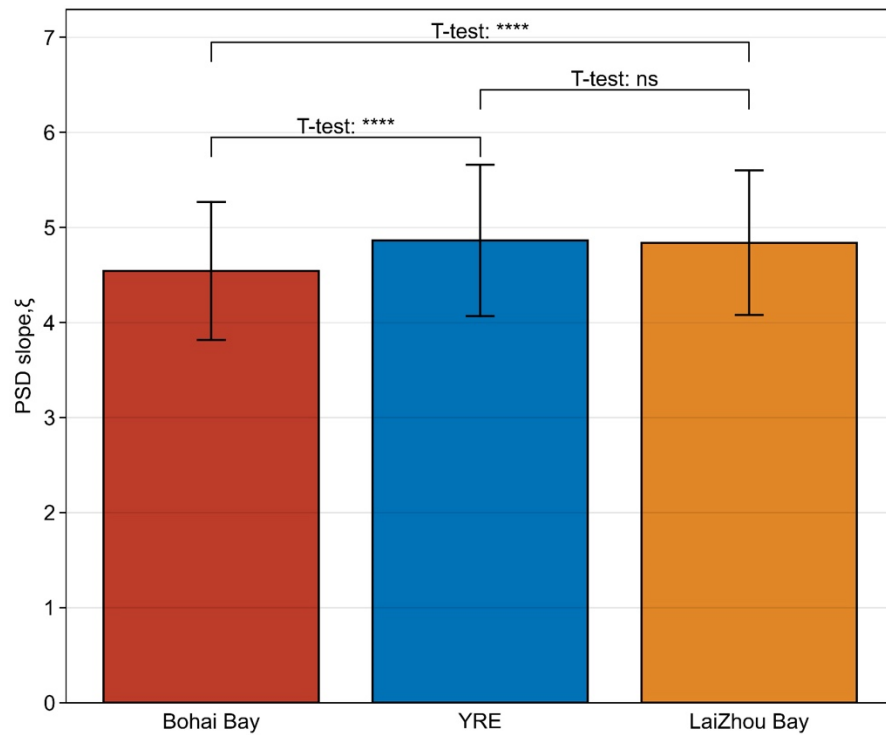


Figure 5. Monthly ANOVA analysis among the Bohai Bay, the front of the YRD and Laizhou Bay. T-test “****” denotes the p -value ≤ 0.0001 , “ns” represents no significant difference.

3.3. PSD Slope, ζ , during Extreme Flood Events

The discharge and sediment load of the Yellow River can influence ζ to some extent. Here, we select the water-regulation flood (WSRS) of summer of 2019 and the Autumn flood in 2021 to investigate ζ changes in a short period (Figure 6). A river plume with a low ζ around 3.0 was localized to the south of the Yellow River on 23 June. On this date, the Yellow River discharge was $730 \text{ m}^3/\text{s}$, while the suspended concentration was $1.7 \text{ kg}/\text{m}^3$ at the LiJin Station (Figure 6b). The area with low ζ gradually increased over time because of the large volume of fresh water emptying into the Bohai Sea. ζ approached 4 along the entire Yellow River Delta shoreline on 1 July 2019. The particle size slope ζ returned to normal values on 24 July 2019 once the WSRS ended.

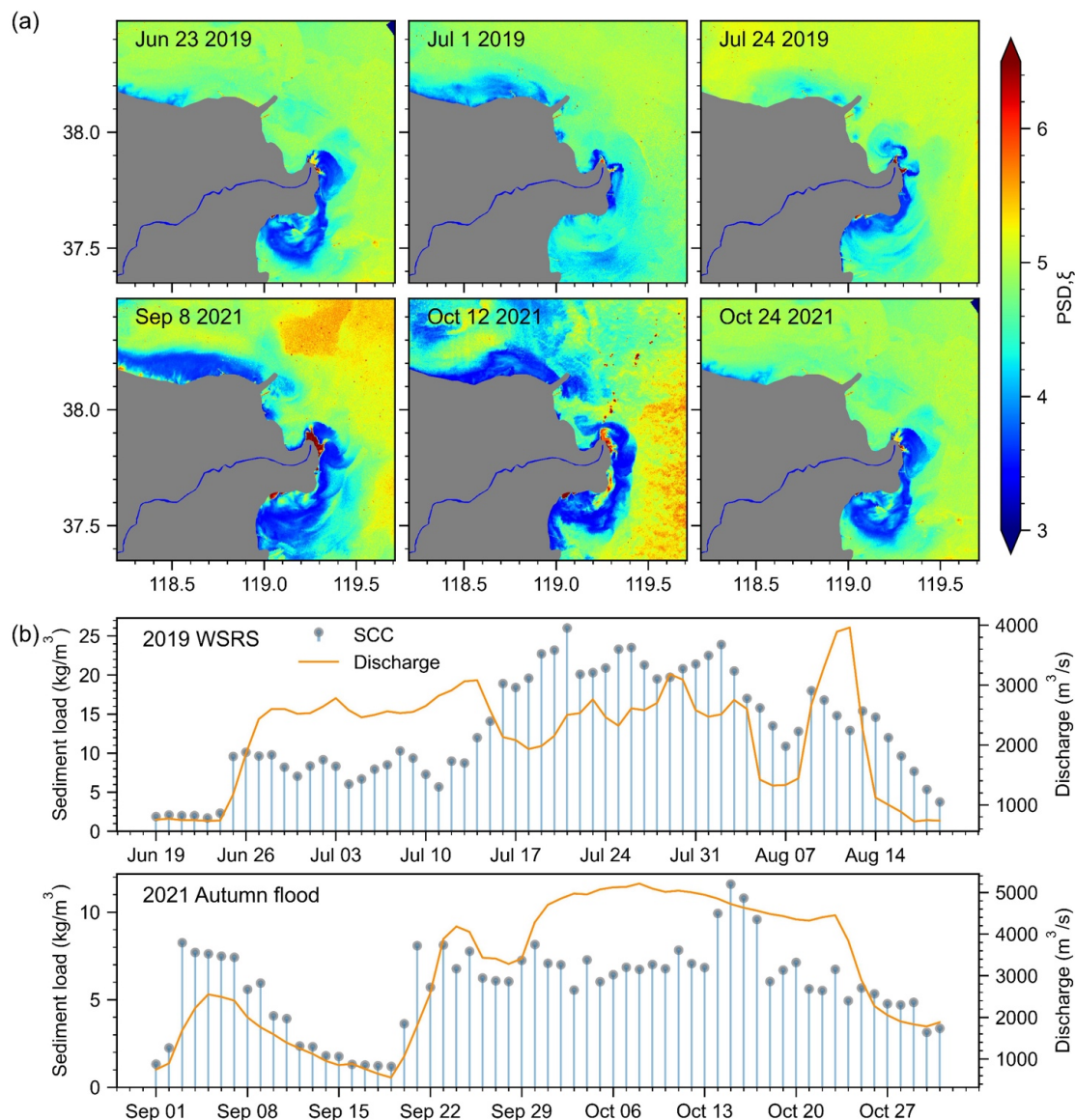


Figure 6. PSD variations during flood events. (a) Regulated flood (WSRS) in 2019 and autumn flood in 2021. (b) Sediment loads and discharge at the LiJin station for the WSRS and autumn floods.

A historic autumn flood lasting 60 days occurred in the Yellow River drainage basin from September to October of 2021. During this extreme flood, sediments debouched from the river mouth and flowed north and south along the coast, forming a band with a low value of ζ (Figure 6a). The river sediment concentration and discharge were $5.59 \text{ kg}/\text{m}^3$ and $2000 \text{ m}^3/\text{s}$ on 8 September 2021 and both reduced to $2.36 \text{ kg}/\text{m}^3$ and $1250 \text{ m}^3/\text{s}$ on

12 October 2021. Influenced by the sediment deluge, ζ became less than 3.5. Then, river discharge decreased with ζ increasing after 20 October.

3.4. Time Series Decomposition of the PSD Slope, ζ

The PSD slope, ζ , displays significant temporal variations at annual and seasonal scales in the YRD (Figure 7). The ζ oscillates from 3.7 to 5.5 in each year with the highest value reached in June 2020. The trend component of the ζ increased from -0.5 to 0 between 2016 and 2022. The seasonality of particle size characteristics is strong. The seasonal component of ζ is lower than -0.5 in the wintertime and reaches 0.5 in the warm season. The residual component is essentially consistent with the anomaly, with discrepancies present both at the monthly and annual scales. For example, the residual of the ζ was relatively smooth in 2019 and 2022, which is in accordance with the ζ maps (Figure 3).

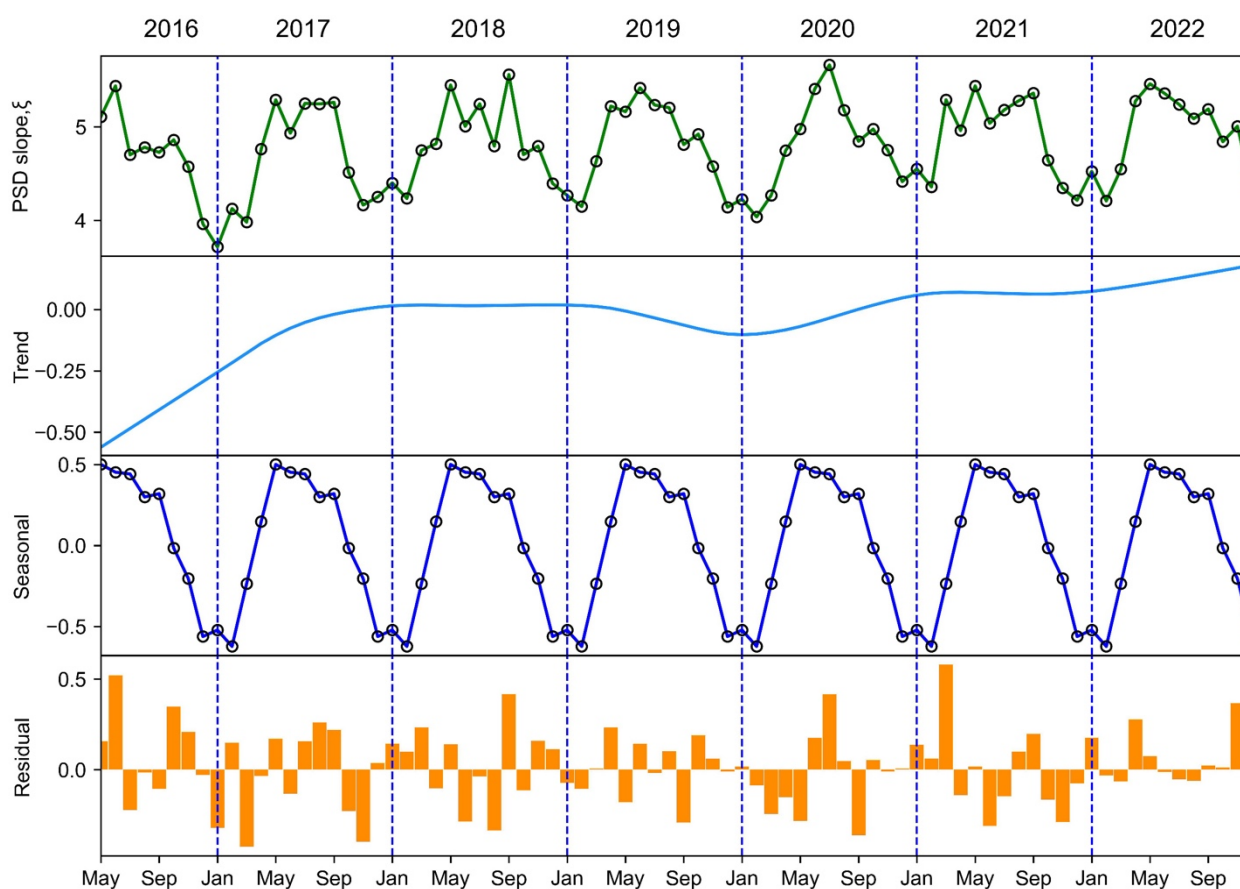


Figure 7. Time series decomposition of the PSD slope, ζ , from 2016 to 2022. ζ is mean value of the whole study area.

According to the distribution of ζ , SST, SSH and wind applied by the low-pass filter with a 0.2 filter frequency in the last six years, particle size is very sensitive to surrounding environmental changes (Figure 8). It is clear that the PSD slope, ζ , dynamically interacts with the oceanic forcing parameters from low-frequency measurements. The fluctuation trend of the ζ (4.5–5.5) is similar to SST ($5\text{ }^{\circ}\text{C}$ – $20\text{ }^{\circ}\text{C}$) and SSH (0.1 m–0.3 m) when wave crests occur in the warm season and troughs occur in the cold season. However, the component of wind speed behaves following an opposite trend compared to other three variables. The highest wind reached 6.5 m/s in January 2018 and the lowest wind was 5.0 m/s in July 2017.

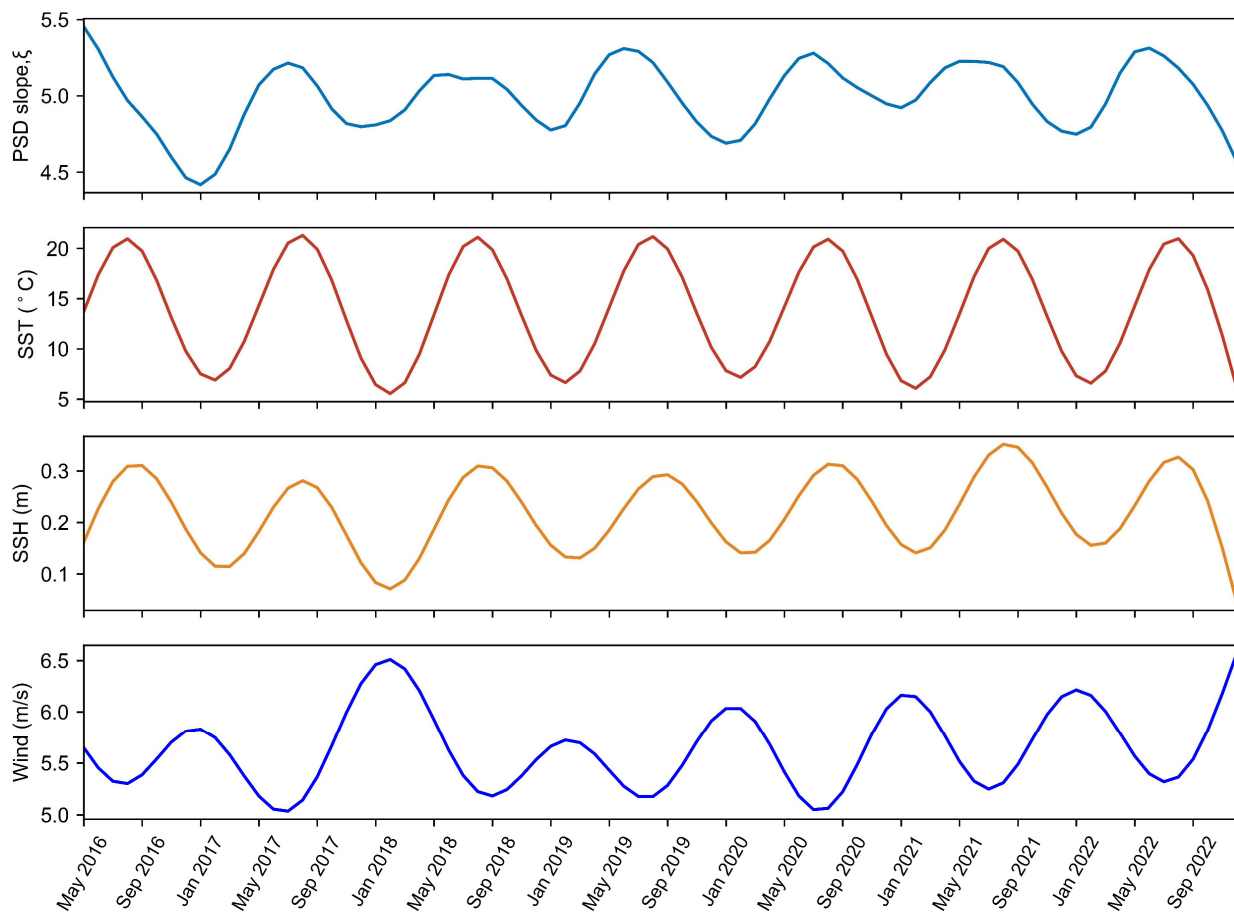


Figure 8. Variation in the PSD slope, ζ and SST, SSH and Wind using a low-pass filter from 2016 to 2022.

3.5. Inorganic Sediments Dominate SPM Mapping Based on the PSD Slope, ζ

We can attempt to discriminate the dominant particle characteristics depending on the value of the ζ . Many empirical algorithms have been developed to retrieve suspended particle matter (SPM) in the YRD [54,55]. Here, we used estimates of SPM obtained by the ratio of red and green wavelengths in the Sentinel-3 A/B OLCI images. The SPM was derived using the following equation: $\log(\text{SPM}) = 4.289 \times R_{rs}(670)/R_{rs}(555) + 0.0667$ [56]. The SPM spatial pattern changes significantly in different seasons, and it is often specular to the particle size distribution (Figure 9a). For example, SPM exceeds 90 mg L^{-1} in Bohai Bay in the winter season (December, January and February) while the value of ζ remains low and close to 3.5. Similar patterns are also present in the other three seasons, with a low value of ζ related to high sediment concentrations. In this study, we defined areas with $\zeta < 4.6$ as inorganic-dominated SPM (InSPM) and this value was chosen through multiple trials (Figure 9b). The InSPM nearly accounts for half of the YRE in winter, and the area is relatively small in other seasons. Too large or too small a threshold of ζ may result in InSPM area changes, here we just selected a comprise value. Furthermore, we calculated the InSPM area from 2016 to 2022 (Figure 9c). The maximum area of InSPM was in January and February 2016 ($51,287$ and $45,392 \text{ km}^2$, respectively). The mean InSPM area in winter approached $23,900 \text{ km}^2$. High wind speeds and low SST lead to much more inorganic SPM in the water column in this period. The spatiotemporal dynamics of ζ near the YRD also provide us with insight as to sediment transport mechanism variations over the course of the year.

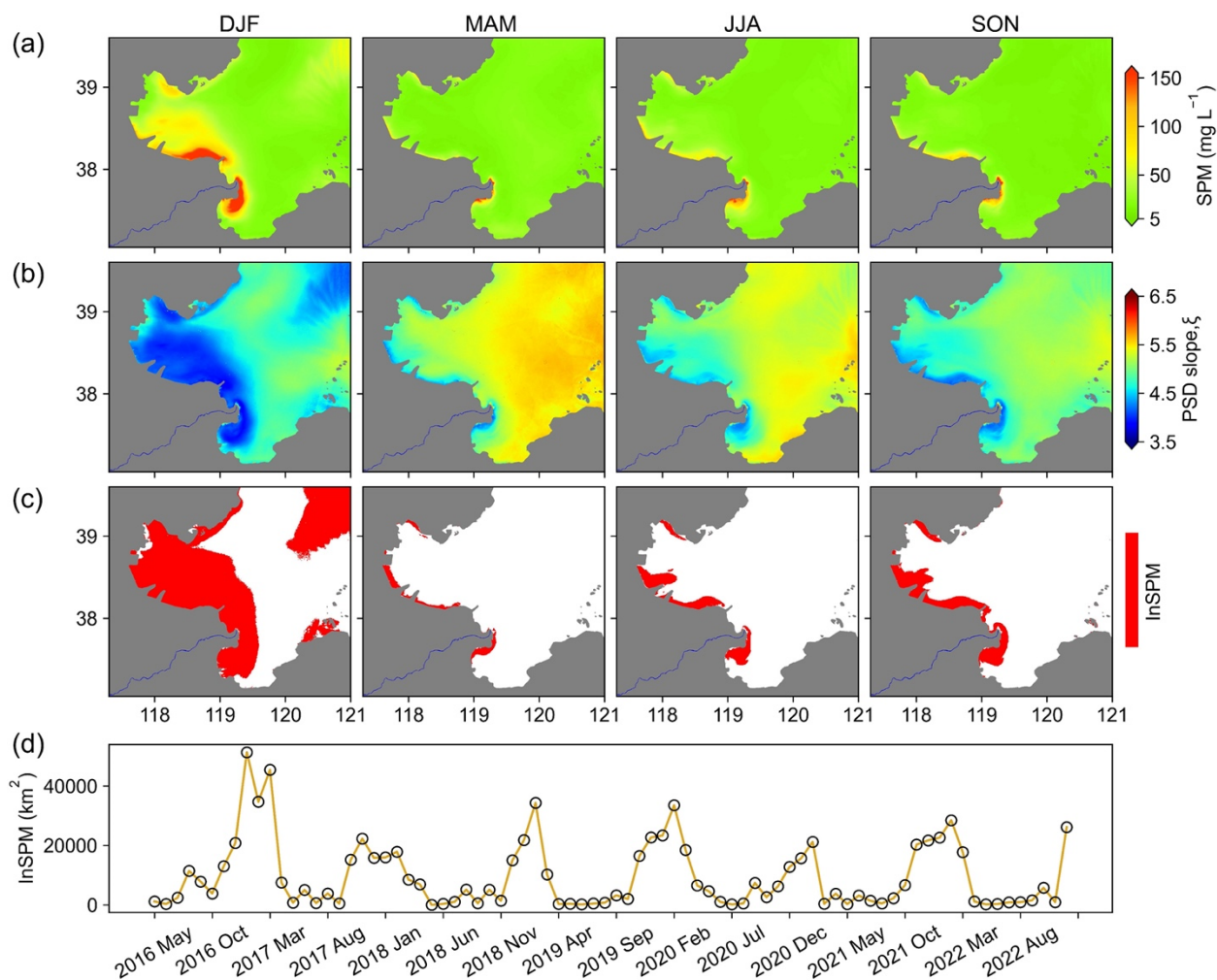


Figure 9. Inorganic-dominated SPM extract based on the PSD slope, ζ . (a–c) represent Winter (December, January and February), Spring (March, April and May), Summer (June, July and August) and Autumn (September, October and November). (d) Area of inorganic-dominated SPM from 2016 to 2022.

4. Discussion

4.1. Estimation of PSD Slope, ζ , Maps in the YRD Using Remote Sensing

PSD slope, ζ , maps derived from remote sensing images provide a quantitative assessment of sediment dynamics in shallow bay environments [7,57]. For coastal zones, only remote sensing with moderate spatial resolution and a high revisit time can fully capture the ζ in the surface waters. We compiled all the ζ from Sentinel-3A/B OLCI imagery. Our study shows that ζ displays a rising trend in Bohai Sea, indicating that the fraction of fine particles is gradually decreasing.

The presence of an onshore to offshore particle size gradient occurs in Bohai Sea [58]. The deposition and resuspension of sediments may influence the size of the particles, and the YRD waters are an effective trap for fine-grain cohesive sediment, leading to an area of high SPM concentration [59]. Considering inorganic particles (dominated by clay, silt) are mainly confined to shallow waters, the ζ is relatively small along the coast [60,61]. Then, a higher negative correlation between the ζ and SPM concentration occurs in the areas near the delta ($R^2 = 0.51$) in Figure 10. ζ values below 4.5 correspond to high SPM concentrations ($>60 \text{ mg L}^{-1}$), and vice versa. In addition, organic-dominated particles are easy to control the aggregate size, because the organic components can be sticky as large aggregates [62]. Therefore, the average of the ζ in offshore waters is at least one more than the particle size along the Yellow River shoreline (Figure 2). As a result, the correction of the ζ and SPM

reaches 0.41 in areas away from the delta (Figure 10). In regard to offshore seas, both of them have no obvious correlation ($R^2 = 0.001$). This is because particle size can affect the transition between particles' cohesive and noncohesive behavior and, therefore, influence SPM concentration [53].

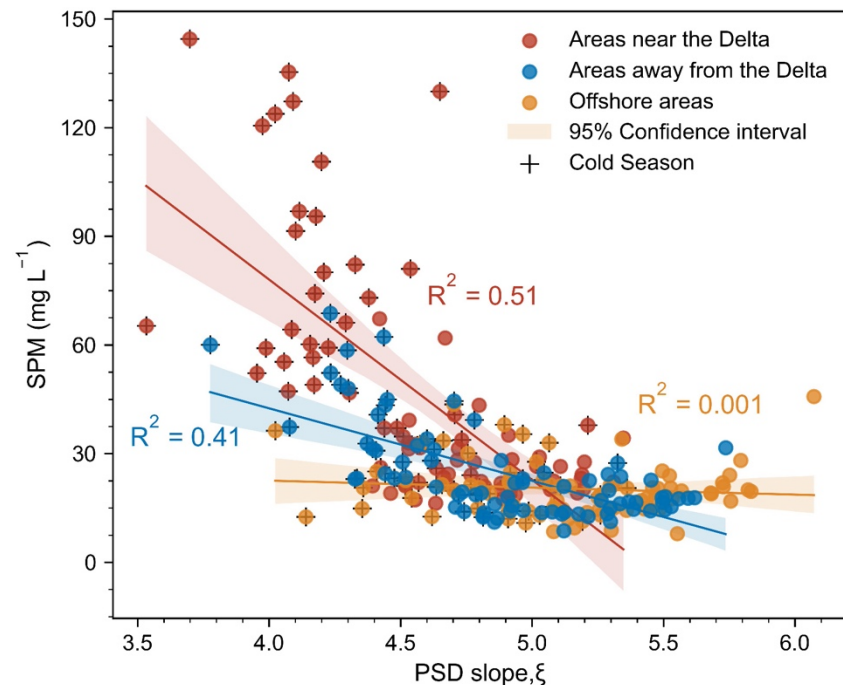


Figure 10. Relationship between monthly mean PSD slope, ζ , and SPM in different region away from the YRD during 2016 to 2022.

Seasonal variation in particle size occurs, with large values of the slope in the warm season and small values in the cold period (Figure 4). The correlation between the ζ and SPM in the cold season is much more obvious than during the rest of the year (Figure 10). Particle floc and settling velocity may cause a seasonal change in the ζ and SPM [63]. Small inorganic flocs and low settling velocities occur in the winter and larger flocs as well as higher settling velocities occur in the summer [53]. Therefore, seasonal ζ dynamics are directly related to local physical and biological process.

4.2. Driving Factors for the Dynamics of the PSD Slope, ζ

Human activity and extreme weather events may significantly drive particle characteristics over a short timeframe. The WSRS is an unprecedented engineering effort to regulate the water–sediment environment of the Yellow River since 2002. It mitigates the siltation in the lower river channel through dam-regulated flood water over 20 days from mid-June to early July [31]. The WSRS is split into two phases, in the first stage, water is released from the Xiaolangdi Reservoir, while in the second phase, sediments are flushed from the reservoir [33]. During dam operations, a large amount of fresh water pours into Bohai Sea, where the particle composition begins to change. The ζ values during this period are higher than normal. For example, the ζ is 4.4 on 1 July 2019 after the release of water from the dam in contrast to the typical value of 3.2 on 23 June 2019 (Figure 6). In the second phase, a large volume of fine sediments (silt and clay) is released from the reservoir bottom producing a sediment load with a concentration of 20 kg/m^3 at the LiJin station. At that time, the particle size is nearly $80 \mu\text{m}$ in the LiJin section [64]. During this phase, the particles become finer, as indicated by a ζ range from 3 to 4.5 on 24 July 2019. The discharge and sediment load vary dramatically during this phase, reducing the values of ζ to 3–4 along the YRD.

Environmental driving factors, including river sediment load, wind–wave induced sediment resuspension and water temperature can influence the distribution of ζ [65].

The ζ exhibits significant variations during a storm surge when strong winds and waves resuspend large volumes of small particles in surface waters [24]. The PSD slope, ζ , increases with SST, with a correlation coefficient of $R^2 = 0.41$ (Figure 11a). The SST leads to the termination of surface spring blooms in the Bohai Sea [66] and phytoplankton biomass grows when the sea temperature rises [58]. Wind speed and the sea-surface height also have a significant effect on ζ . The R-square is nearly 0.27 between ζ and SSH and 0.36 between ζ and wind (Figure 11b,c). High SSH mainly occurs in the spring and summer, and ζ increases a little with SSH, but with a low correlation coefficient. Strong wind can increase wave energy, which stirs the particle distribution and brings bottom sediment into the upper water column [53]. As a result, there is a reverse correlation between ζ and wind speed.

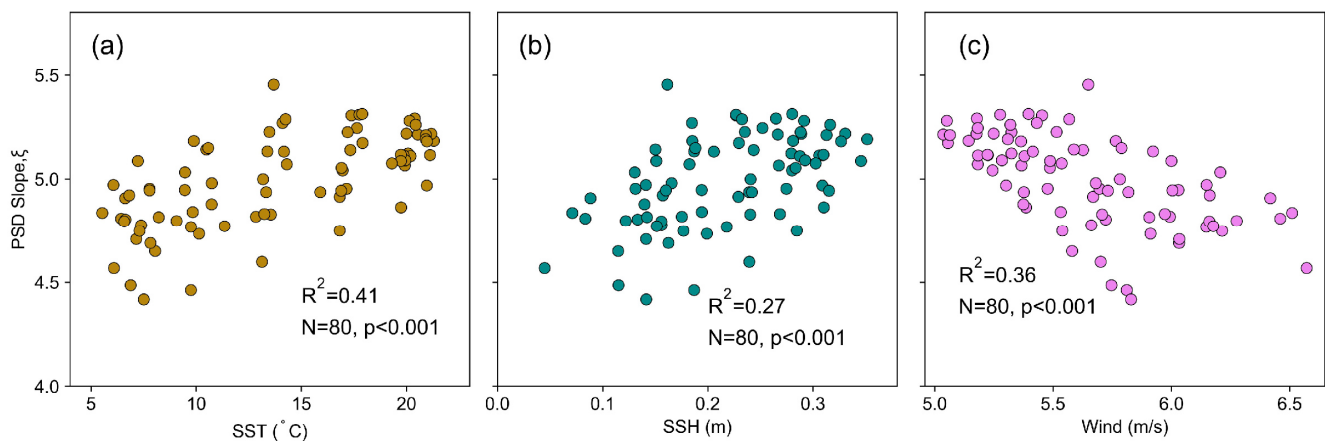


Figure 11. Relationship between driving factors and particle size slope, ζ , on a monthly scale. (a) Correlation between sea surface temperature (SST) and ζ . (b) Correlation between sea surface height (SSH) and ζ . (c) Correlation between wind and ζ . Note that the particle size slope, ζ , SST, SSH and wind are implemented using a low-pass filter.

4.3. Uncertainty in the PSD Slope, ζ Inversion

The approximation in deriving the IOP parameter based on $a_w(\lambda)$ in the NIR wavelength is higher than for other constituent absorption coefficients for most waters [15,43]. Although $a_d(\lambda)$ may be a non-negligible parameter in the NIR bands in extremely turbid waters, $b_b(\lambda)/(a(\lambda) + b_b(\lambda))$ is approximated to 1 as $b_b(\lambda)$ is much larger than $a(\lambda)$. At the same time, the difference between $b_b(\lambda)/(a(\lambda) + b_b(\lambda))$ and $b_b(\lambda)/(a_w(\lambda) + b_b(\lambda))$ is less than 0.005% in Case 2 waters [21,67]. The power law slope η obtained from $b_{bp}(\lambda)$ using two NIR wavelengths can distinguish the spectral relationships for $b_{bp}(\lambda)$ at different Sentinel-3A/B OLCI bands. Conversely, the power law fit of $b_{bp}(\lambda)$ performs poorly in coastal waters because of strong particle absorption in the blue wavelength [17]. However, the η values are accurate for NIR wavelengths. Therefore, the $b_{bp}(\lambda)$ can be derived at the two NIR wavelengths with good accuracy [4,68]. Mie scattering yields reasonable estimates of the PSD slope, ζ , and backscattering ratio, b_{bp} , even with possible uncertainty when the particle bulk refractive index, n_p , is chosen (Figure 12). The uncertainties of ζ derived from the Mie scattering simulation are nearly 0.2. The uncertainty in ζ is nearly 15% of the total value from ocean color data [21]. Therefore, the satellite-based retrievals of ζ match the limited field samplings well [17].

Equation (8) combining η and ζ is calculated using the Mie scattering simulations, where particles are regarded as homogeneous spherical particles [43]. This assumption is often too simple in highly turbid coastal waters, which can lead to the underestimation of backscattering. This will bring some uncertainties and errors from the satellite-derived ζ . Generally, the backscattering of spheres is thought to be $\sim 10\%$ and even slightly larger than the backscattering from an equal volume spherical particles [42]. In addition, the particle refractive index and particle aspect ratio also contribute to particle scattering in coastal

waters. Thus, it means that uncertainty from the Mie scattering simulations also depends on refractive index and particle aspect ratio. However, η is computed from $b_{bp}(\lambda)/b_{bp}(\lambda_0)$, and the possible biases of η and ζ are largely reduced owing to the fact that they balance each other in the ratio of $b_{bp}(\lambda)/b_{bp}(\lambda_0)$ [21].

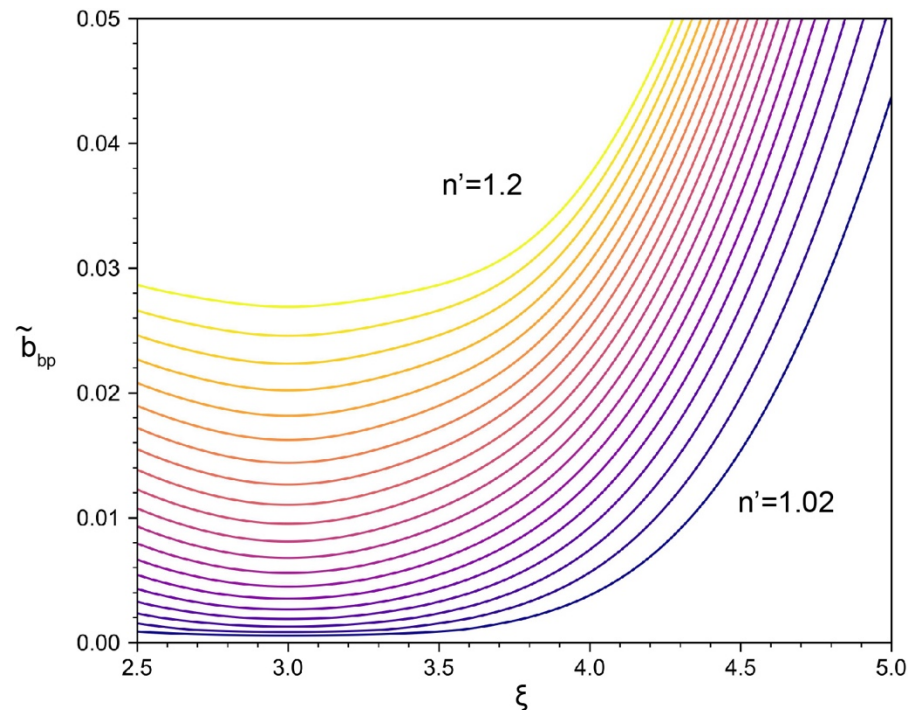


Figure 12. Mie theory of the backscattering ratio $\tilde{b}_{bp}(\lambda)$ as a function of ζ in response to imaginary part ranges from 1.02 to 1.2 [12].

5. Conclusions

Particle size is the second order of suspended particle matter properties, and it remains a challenge to accurately extract it. In this study, we introduced an empirical model to indirectly estimate particle sizes in the Yellow River delta based on the slope of particle backscattering ($b_{bp}(\lambda)$) at NIR wavelengths. Seasonal and interannual variations in the ζ along the Yellow River Delta are characterized in detail using the Sentinel-3A/B OLCI from the last six years (2016–2022). Here, we detected a slight increase in ζ in the last six years (the trend component of the time series changed from -0.5 to 0 from 2016 to 2022), indicating that suspended particles are, on average, increasing in size. Considering that the ζ can indicate particle composition, areas dominated by inorganic particles are obtained using the magnitude of ζ . A small ζ indicates that more inorganic particles occur. The relationship between the SPM and the ζ continues to decrease with increasing distance from shore in our study area. These results give us a general outline of how and why the particle size changes in the Yellow River Delta. With the quick changes in the global marine environment, the regional and temporal variability of the ζ will help us to better quantify the dynamics of suspended particles, monitor the marine ecosystem and comprehend the physical and biogeochemical dynamics of the Yellow River delta, which can further improve our understanding of the system.

Author Contributions: S.J. and S.F. conceived and designed the framework of this research; S.J. and S.F. performed the experiments and wrote the paper; S.J. analyzed the data; T.Z. and X.Z. gave comments, suggestions to the manuscript; Q.X. checked the writing and provided many helpful suggestions. All authors have read and agreed to the published version of the manuscript.

Funding: This study was supported by the National Natural Science Foundation of China (U2106211), the Natural Science Foundation of Shandong Province (ZR2022QD123, ZR2020QD092), China Postdoctoral Science Foundation (2021M703245), National Key R&D Program of China (2022FY100300), High-Performance Computing Platform and Seed project (YICE351030601) of Yantai Institute of Coastal Zone Research, Chinese Academy of Sciences. Sampling is supported by “Lanhai101” implementing the open research cruise NORC2023-01(42249901). S.F. was partly supported by the Virginia Coast Reserve Long-Term Ecological Research Program (NSF DEB-1832221) and by the Plum Island Ecosystems Long-Term Ecological Research Program (NSF OCE-2224608).

Data Availability Statement: Data are contained within the article.

Acknowledgments: We also thank European Space Agency for providing Sentinel-3A/B OLCI images. The authors would like to thank the reviewers and the editor for their constructive comments.

Conflicts of Interest: The authors declare that the research was conducted in the absence of any commercial or financial relationships that could be construed as a potential conflict of interest.

References

1. Reynolds, R.A.; Stramski, D.; Wright, V.M.; Woźniak, S.B. Measurements and characterization of particle size distributions in coastal waters. *J. Geophys. Res. Oceans* **2010**, *115*, C08024. [[CrossRef](#)]
2. Forero Lopez, A.D.; Truchet, D.M.; Rimondino, G.N.; Maisano, L.; Spetter, C.V.; Buzzi, N.S.; Nazzarro, M.S.; Malanca, F.E.; Furlong, O.; Fernandez Severini, M.D. Microplastics and suspended particles in a strongly impacted coastal environment: Composition, abundance, surface texture, and interaction with metal ions. *Sci. Total Environ.* **2021**, *754*, 142413. [[CrossRef](#)]
3. Zheng, G.; DiGiacomo, P.M.; Kaushal, S.S.; Yuen-Murphy, M.A.; Duan, S. Evolution of Sediment Plumes in the Chesapeake Bay and Implications of Climate Variability. *Environ. Sci. Technol.* **2015**, *49*, 6494–6503. [[CrossRef](#)] [[PubMed](#)]
4. Sun, D.; Qiu, Z.; Hu, C.; Wang, S.; Wang, L.; Zheng, L.; Peng, T.; He, Y. A hybrid method to estimate suspended particle sizes from satellite measurements over Bohai Sea and Yellow Sea. *J. Geophys. Res. Oceans* **2016**, *121*, 6742–6761. [[CrossRef](#)]
5. Woźniak, S.B.; Stramski, D. Modeling the optical properties of mineral particles suspended in seawater and their influence on ocean reflectance and chlorophyll estimation from remote sensing algorithms. *Appl. Opt.* **2004**, *43*, 3489–3503. [[CrossRef](#)] [[PubMed](#)]
6. Quéré, C.L.; Harrison, S.P.; Colin Prentice, I.; Buitenhuis, E.T.; Aumont, O.; Bopp, L.; Claustre, H.; Cotrim Da Cunha, L.; Geider, R.; Giraud, X.; et al. Ecosystem dynamics based on plankton functional types for global ocean biogeochemistry models. *Glob. Chang. Biol.* **2005**, *11*, 2016–2040. [[CrossRef](#)]
7. Reynolds, R.A.; Stramski, D. Variability in Oceanic Particle Size Distributions and Estimation of Size Class Contributions Using a Non-parametric Approach. *J. Geophys. Res. Oceans* **2021**, *126*, e2021JC017946. [[CrossRef](#)]
8. Kang, L.; He, Y.; Dai, L.; He, Q.; Ai, H.; Yang, G.; Liu, M.; Jiang, W.; Li, H. Interactions between suspended particulate matter and algal cells contributed to the reconstruction of phytoplankton communities in turbulent waters. *Water Res.* **2019**, *149*, 251–262. [[CrossRef](#)]
9. Sutherland, K.R.; Madin, L.P.; Stocker, R. Filtration of submicrometer particles by pelagic tunicates. *Proc. Natl. Acad. Sci. USA* **2010**, *107*, 15129–15134. [[CrossRef](#)]
10. Kostadinov, T.S.; Siegel, D.A.; Maritorena, S.; Guillocheau, N. Optical assessment of particle size and composition in the Santa Barbara Channel, California. *Appl. Opt.* **2012**, *51*, 3171–3189. [[CrossRef](#)]
11. Jonasz, M.; Fournier, G.R. *Light Scattering by Particles in Water: Theoretical and Experimental Foundations*; Academic Press: New York, NY, USA, 2007.
12. Twardowski, M.S.; Boss, E.; Macdonald, J.B.; Pegau, W.S.; Barnard, A.H.; Zaneveld, J.R.V. A model for estimating bulk refractive index from the optical backscattering ratio and the implications for understanding particle composition in case I and case II waters. *J. Geophys. Res. Oceans* **2001**, *106*, 14129–14142. [[CrossRef](#)]
13. Fujii, H.; Ueno, M.; Inoue, Y.; Aoki, T.; Kobayashi, K.; Watanabe, M. Model equations of light scattering properties and a characteristic time of light propagation for polydisperse colloidal suspensions at different volume fractions. *Opt. Express.* **2022**, *30*, 3538–3552. [[CrossRef](#)]
14. Bader, H. The hyperbolic distribution of particle sizes. *J. Geophys. Res.* **1970**, *75*, 2822–2830. [[CrossRef](#)]
15. Babin, M.; Morel, A.; Fournier-Sicre, V.; Fell, F.; Stramski, D. Light scattering properties of marine particles in coastal and open ocean waters as related to the particle mass concentration. *Limnol. Oceanogr.* **2003**, *48*, 843–859. [[CrossRef](#)]
16. Buonassissi, C.J.; Dierssen, H.M. A regional comparison of particle size distributions and the power law approximation in oceanic and estuarine surface waters. *J. Geophys. Res. Oceans* **2010**, *115*, C10028. [[CrossRef](#)]
17. Kostadinov, T.S.; Siegel, D.A.; Maritorena, S. Retrieval of the particle size distribution from satellite ocean color observations. *J. Geophys. Res. Oceans* **2009**, *114*, C09015. [[CrossRef](#)]
18. Boss, E.; Twardowski, M.S.; Herring, S. Shape of the particulate beam attenuation spectrum and its inversion to obtain the shape of the particulate size distribution. *Appl. Opt.* **2001**, *40*, 4885–4893. [[CrossRef](#)]

19. Diehl, P.; Haardt, H. Measurement of the spectral attenuation to support biological-research in a plankton tube experiment. *Oceanol. Acta* **1980**, *3*, 89–96.
20. Slade, W.H.; Boss, E. Spectral attenuation and backscattering as indicators of average particle size. *Appl. Opt.* **2015**, *54*, 7264–7277. [[CrossRef](#)]
21. Shi, W.; Wang, M. Characterization of Suspended Particle Size Distribution in Global Highly Turbid Waters from VIIRS Measurements. *J. Geophys. Res. Oceans* **2019**, *124*, 3796–3817. [[CrossRef](#)]
22. Loisel, H.; Nicolas, J.-M.; Sciandra, A.; Stramski, D.; Poteau, A. Spectral dependency of optical backscattering by marine particles from satellite remote sensing of the global ocean. *J. Geophys. Res. Oceans* **2006**, *111*, C09024. [[CrossRef](#)]
23. Stramski, D.; Bricaud, A.; Morel, A. Modeling the inherent optical properties of the ocean based on the detailed composition of the planktonic community. *Appl. Opt.* **2001**, *40*, 2929–2945. [[CrossRef](#)] [[PubMed](#)]
24. Liu, Y.; Huang, H.; Yan, L.; Yang, X.; Bi, H.; Zhang, Z. Particle Size Parameters of Particulate Matter Suspended in Coastal Waters and Their Use as Indicators of Typhoon Influence. *Remote Sens.* **2020**, *12*, 2581. [[CrossRef](#)]
25. Lei, S.; Xu, J.; Li, Y.; Li, L.; Lyu, H.; Liu, G.; Chen, Y.; Lu, C.; Tian, C.; Jiao, W. A semi-analytical algorithm for deriving the particle size distribution slope of turbid inland water based on OLCI data: A case study in Lake Hongze. *Environ. Pollut.* **2021**, *270*, 116288. [[CrossRef](#)] [[PubMed](#)]
26. Renosh, P.R.; Schmitt, F.G.; Loisel, H.; Sentchev, A.; Mériaux, X. High frequency variability of particle size distribution and its dependency on turbulence over the sea bottom during re-suspension processes. *Cont. Shelf Res.* **2014**, *77*, 51–60. [[CrossRef](#)]
27. Recuero Virto, L. A preliminary assessment of the indicators for Sustainable Development Goal (SDG) 14 “Conserve and sustainably use the oceans, seas and marine resources for sustainable development”. *Mar. Policy* **2018**, *98*, 47–57. [[CrossRef](#)]
28. Fagherazzi, S.; Palermo, C.; Rulli, M.C.; Carniello, L.; Defina, A. Wind waves in shallow microtidal basins and the dynamic equilibrium of tidal flats. *J. Geophys. Res. Earth* **2007**, *112*, F02024. [[CrossRef](#)]
29. Lv, X.; Yuan, D.; Ma, X.; Tao, J. Wave characteristics analysis in Bohai Sea based on ECMWF wind field. *Ocean Eng.* **2014**, *91*, 159–171. [[CrossRef](#)]
30. Wang, H.; Yang, Z.; Li, Y.; Guo, Z.; Sun, X.; Wang, Y. Dispersal pattern of suspended sediment in the shear frontal zone off the Huanghe (Yellow River) mouth. *Cont. Shelf Res.* **2007**, *27*, 854–871. [[CrossRef](#)]
31. Wang, A.; Wang, H.; Bi, N.; Wu, X. Sediment Transport and Dispersal Pattern from the Bohai Sea to the Yellow Sea. *J. Coastal Res.* **2016**, *2016*, 104–116. [[CrossRef](#)]
32. Yang, S.L.; Shi, B.; Fan, J.; Luo, X.; Tian, Q.; Yang, H.; Chen, S.; Zhang, Y.; Zhang, S.; Shi, X.; et al. Streamflow Decline in the Yellow River along with Socioeconomic Development: Past and Future. *Water* **2020**, *12*, 823. [[CrossRef](#)]
33. Wang, H.; Wu, X.; Bi, N.; Li, S.; Yuan, P.; Wang, A.; Syvitski, J.P.M.; Saito, Y.; Yang, Z.; Liu, S.; et al. Impacts of the dam-orientated water-sediment regulation scheme on the lower reaches and delta of the Yellow River (Huanghe): A review. *Glob. Planet. Change* **2017**, *157*, 93–113. [[CrossRef](#)]
34. Ren, M.-E.; Shi, Y.-L. Sediment discharge of the Yellow River (China) and its effect on the sedimentation of the Bohai and the Yellow Sea. *Cont. Shelf Res.* **1986**, *6*, 785–810. [[CrossRef](#)]
35. Yuan, P.; Wang, H.; Wu, X.; Bi, N. Grain-Size Distribution of Surface Sediments in the Bohai Sea and the Northern Yellow Sea: Sediment Supply and Hydrodynamics. *J. Ocean China* **2020**, *19*, 589–600. [[CrossRef](#)]
36. Cazzaniga, I.; Bresciani, M.; Colombo, R.; Della Bella, V.; Padula, R.; Giardino, C. A comparison of Sentinel-3-OLCI and Sentinel-2-MSI-derived Chlorophyll-a maps for two large Italian lakes. *Remote Sens. Lett.* **2019**, *10*, 978–987. [[CrossRef](#)]
37. Vanhellemont, Q.; Ruddick, K. Atmospheric correction of Sentinel-3/OLCI data for mapping of suspended particulate matter and chlorophyll-a concentration in Belgian turbid coastal waters. *Remote Sens. Environ.* **2021**, *256*, 112284. [[CrossRef](#)]
38. Zhang, X.; Fichot, C.G.; Baracco, C.; Guo, R.; Neugebauer, S.; Bengtsson, Z.; Ganju, N.; Fagherazzi, S. Determining the drivers of suspended sediment dynamics in tidal marsh-influenced estuaries using high-resolution ocean color remote sensing. *Remote Sens. Environ.* **2020**, *240*, 111682. [[CrossRef](#)]
39. Zhou, Y.; Yu, D.; Cheng, W.; Gai, Y.; Yao, H.; Yang, L.; Pan, S. Monitoring multi-temporal and spatial variations of water transparency in the Jiaozhou Bay using GOCI data. *Mar. Pollut. Bull.* **2022**, *180*, 113815. [[CrossRef](#)] [[PubMed](#)]
40. Liu, X.; Qiao, L.; Zhong, Y.; Wan, X.; Xue, W.; Liu, P. Pathways of suspended sediments transported from the Yellow River mouth to the Bohai Sea and Yellow Sea. *Estuar. Coast. Shelf Sci.* **2020**, *236*, 106639. [[CrossRef](#)]
41. Morel, A. In-water and remote measurements of ocean color. *Bound-Lay Meteorol.* **1980**, *18*, 177–201. [[CrossRef](#)]
42. van de Hulst, H.C. *Light Scattering by Small Particles*; Dover: New York, NY, USA, 1981.
43. Mobley, C. *Light and Water: Radiative Transfer in Natural Waters*; Academic Press: New York, NY, USA, 1994.
44. Doxaran, D.; Ruddick, K.; McKee, D.; Gentili, B.; Tailliez, D.; Chami, M.; Babin, M. Spectral variations of light scattering by marine particles in coastal waters, from the visible to the near infrared. *Limnol. Oceanogr.* **2009**, *54*, 1257–1271. [[CrossRef](#)]
45. Pinet, S.; Martinez, J.-M.; Ouillon, S.; Lartiges, B.; Villar, R.E. Variability of apparent and inherent optical properties of sediment-laden waters in large river basins: Lessons from in situ measurements and bio-optical modeling. *Opt. Express.* **2017**, *25*, A283–A310. [[CrossRef](#)] [[PubMed](#)]
46. Forget, P.; Ouillon, S.; Lahet, F.; Broche, P. Inversion of Reflectance Spectra of Nonchlorophyllous Turbid Coastal Waters. *Remote Sens. Environ.* **1999**, *68*, 264–272. [[CrossRef](#)]
47. Boss, E.; Pegau, W.S.; Lee, M.; Twardowski, M.; Shybanov, E.; Korotaev, G.; Baratange, F. Particulate backscattering ratio at LEO 15 and its use to study particle composition and distribution. *J. Geophys. Res. Oceans* **2004**, *109*, C01014. [[CrossRef](#)]

48. Gordon, H.R.; Morel, A. *Remote Assessment of Ocean Color for Interpretation of Satellite Visible Imagery: A Review*; Springer: New York, NY, USA, 1983.
49. Doron, M.; Bélanger, S.; Doxaran, D.; Babin, M. Spectral variations in the near-infrared ocean reflectance. *Remote Sens. Environ.* **2011**, *115*, 1617–1631. [[CrossRef](#)]
50. Shi, W.; Wang, M. Ocean reflectance spectra at the red, near-infrared, and shortwave infrared from highly turbid waters: A study in the Bohai Sea, Yellow Sea, and East China Sea. *Limnol. Oceanogr.* **2014**, *59*, 427–444. [[CrossRef](#)]
51. Lee, Z.; Carder, K.L.; Arnone, R.A. Deriving inherent optical properties from water color: A multiband quasi-analytical algorithm for optically deep waters. *Appl. Opt.* **2002**, *41*, 5755–5772. [[CrossRef](#)]
52. Fichtner, F.; Mandery, N.; Wieland, M.; Groth, S.; Martinis, S.; Riedlinger, T. Time-series analysis of Sentinel-1/2 data for flood detection using a discrete global grid system and seasonal decomposition. *Int. J. Appl. Earth Obs.* **2023**, *119*, 103329. [[CrossRef](#)]
53. Fettweis, M.; Baeye, M. Seasonal variation in concentration, size, and settling velocity of muddy marine flocs in the benthic boundary layer. *J. Geophys. Res. Oceans* **2015**, *120*, 5648–5667. [[CrossRef](#)]
54. Zhang, M.; Dong, Q.; Cui, T.; Xue, C.; Zhang, S. Suspended sediment monitoring and assessment for Yellow River estuary from Landsat TM and ETM+ imagery. *Remote Sens. Environ.* **2014**, *146*, 136–147. [[CrossRef](#)]
55. Li, P.; Chen, S.; Ke, Y.; Ji, H.; Li, P.; Fan, Y. Spatiotemporal dynamics of suspended particulate matter in the Bohai Sea, China over the past decade from the space perspective. *Sci. Total Environ.* **2022**, *851*, 158210. [[CrossRef](#)]
56. Jin, S.; Fagherazzi, S.; Fichot, C.G.; Wu, X.; Liu, Y.X.; Zheng, X.; Zou, T.; Xing, Q. Drivers of suspended sediment dynamics along the shorelines of the Yellow River Delta detected from satellite data. *Earth Surf. Proc. Land* **2023**, *48*, 3091–3102. [[CrossRef](#)]
57. Aoki, K.; Furue, R. A model for the size distribution of marine microplastics: A statistical mechanics approach. *PLoS ONE* **2021**, *16*, e0259781. [[CrossRef](#)] [[PubMed](#)]
58. Qing, S.; Zhang, J.; Cui, T.; Bao, Y. Remote sensing retrieval of inorganic suspended particle size in the Bohai Sea. *Cont. Shelf Res.* **2014**, *73*, 64–71. [[CrossRef](#)]
59. Bi, N.; Yang, Z.; Wang, H.; Hu, B.; Ji, Y. Sediment dispersion pattern off the present Huanghe (Yellow River) subdelta and its dynamic mechanism during normal river discharge period. *Estuar. Coast. Shelf Sci.* **2010**, *86*, 352–362. [[CrossRef](#)]
60. Stavn, R.H.; Keen, T.R. Suspended minerogenic particle distributions in high-energy coastal environments: Optical implications. *J. Geophys. Res. Oceans* **2004**, *109*, C05005. [[CrossRef](#)]
61. Hill, P.S.; Boss, E.; Newgard, J.P.; Law, B.A.; Milligan, T.G. Observations of the sensitivity of beam attenuation to particle size in a coastal bottom boundary layer. *J. Geophys. Res. Oceans* **2011**, *116*, C02023. [[CrossRef](#)]
62. Hamm, C.E. Interactive aggregation and sedimentation of diatoms and clay-sized lithogenic material. *Limnol. Oceanogr.* **2022**, *47*, 1790–1795. [[CrossRef](#)]
63. Woźniak, S.B.; Stramski, D.; Stramska, M.; Reynolds, R.A.; Wright, V.M.; Miksic, E.Y.; Cichocka, M.; Cieplak, A.M. Optical variability of seawater in relation to particle concentration, composition, and size distribution in the nearshore marine environment at Imperial Beach, California. *J. Geophys. Res. Oceans* **2010**, *115*, C08027. [[CrossRef](#)]
64. Hou, C.; Yi, Y.; Song, J.; Zhou, Y. Effect of water-sediment regulation operation on sediment grain size and nutrient content in the lower Yellow River. *J. Clean.* **2021**, *279*, 123533. [[CrossRef](#)]
65. Guo, K.; Zou, T.; Jiang, D.; Tang, C.; Zhang, H. Variability of Yellow River turbid plume detected with satellite remote sensing during water-sediment regulation. *Cont. Shelf Res.* **2017**, *135*, 74–85. [[CrossRef](#)]
66. Wang, Z.; Li, W.; Zhang, K.; Agrawal, Y.C.; Huang, H. Observations of the distribution and flocculation of suspended particulate matter in the North Yellow Sea cold water mass. *Cont. Shelf Res.* **2020**, *204*, 104187. [[CrossRef](#)]
67. Stramski, D.; Babin, M.; Woźniak, S.B. Variations in the optical properties of terrigenous mineral-rich particulate matter suspended in seawater. *Limnol. Oceanogr.* **2007**, *52*, 2418–2433. [[CrossRef](#)]
68. Tassan, S.; Ferrari, G.M. Variability of light absorption by aquatic particles in the near-infrared spectral region. *Appl. Opt.* **2003**, *42*, 4802–4810. [[CrossRef](#)]

Disclaimer/Publisher’s Note: The statements, opinions and data contained in all publications are solely those of the individual author(s) and contributor(s) and not of MDPI and/or the editor(s). MDPI and/or the editor(s) disclaim responsibility for any injury to people or property resulting from any ideas, methods, instructions or products referred to in the content.